

NEUE ENERGIEN 2020

Publizierbarer Endbericht – INDEX

Programmsteuerung:

Klima- und Energiefonds

Programmabwicklung:

Österreichische Forschungsförderungsgesellschaft mbH (FFG)

Introduction

The photovoltaic (PV) industry is one of the fastest growing industries. Market analysts foresee no end of growth before 2040. Assuming the current growth pace and moderate state support, 3% of the electricity could be supplied by PV by 2020.

Today, the PV market is dominated by crystalline (c-Si) and poly-crystalline (pc-Si) silicon modules (*1st generation PV*), which are available for many years, are widely accepted from the public and produce reliable power. These mainstream technologies compete with thin film (TF) PV (*2nd generation PV*), from which four types of modules are commercially available: amorphous silicon (a-Si), multijunction thin silicon films (a-Si/ μ c-Si), cadmium telluride (CdTe), copper-indium-gallium-selenide/sulphide (CIGS) and copper-indium selenide/sulphide (CIS). Based on 2010 production figures CdTe is the leading technology. CIGS and a-Si markets also increase their share constantly. TF modules have in general lower efficiencies than c-Si and pc-Si. On the other hand, TF technologies are mostly proprietary, they offer flexibility in terms of substrate (e.g. glass or plastic foils) and show lower cost figures. Nevertheless, with falling raw silicon prices, the profit margins of TF producers are constantly compressed.

In this highly competitive market environment, research is intensified in the direction of new materials, technological processes and designs, in order to come up with PV solutions that could *radically* change the cost schemes, through reduction of production costs and improvement of module performance. Such concepts are known as *3rd generation PV*. In this category fall architectures related to: (i) 3D structures capturing light, (ii) carbon nanotubes, (iii) dye-sensitized solar cells (DSSC), (iv) nanocrystals/quantum dots, (v) organic materials and (vi) concentrated PV.

One of the aforementioned 3rd generation PV approaches, namely the dye-sensitized solar cell¹, offers relatively large efficiencies at lab scale (>10%) and has been intensively investigated for decades. The DSSC is based on metal-organic dyes to absorb sun light and generate electrons, which are transferred through a titania mesoporous network to a transparent electrode and from there to an external load. The dye is regenerated through a back-side liquid electrolyte. The DSSC has not yet achieved the commercialization breakthrough as it suffers from long term stability and encapsulation problems, caused by the employed metal-organic dyes and liquid electrolyte.

Interestingly, the DSSC design has been adapted to concepts employing more stable inorganic materials. For instance, there are reports where semiconductor nanocrystals (NCs) (e.g. CdTe) or extra

thin film absorber (ETA) layers replace the metal-organic dye²⁻⁴, or the liquid electrolyte is replaced by an inorganic hole transport medium (HTM)^{2,3}. Additionally, the titania mesoporous network that traditionally serves as electron transport medium, was attempted to be replaced by ZnO nanowire (NW) arrays⁵, providing the advantage of a direct electrical path between the absorber and the transparent electrode.

The target of the SAN-CELL project was to apply low-cost, easily up-scalable nanofabrication processes to produce material components that could bring such a cell design a step forward. These processes include solution-based fabrication methods such as electrodeposition and hot injection, as well as mainstream vacuum techniques, like sputtering. The intention was to produce self-assembled nanostructures without application of patterning techniques. The targeted material components consist of 3D ZnO nanowire-based transparent electrodes, semiconducting nanocrystals (NCs) with tailored opto-electrical properties and thin film functional layers as absorbers and inorganic hole transport medium as a replacement for the liquid electrolyte used in the DSSC. Special focus was given on the low cost and the low environmental impact of these materials.

More specifically, the project knowledge-based goals have been defined as follows:

- (a) Establish the most promising transparent conducting layer that ensures state-of-the-art electrical and optical properties and at the same time facilitates the ZnO nanowire growth.
- (b) Establish control over ZnO NW morphology.
- (c) Establish the NC and thin film absorber materials that combine appropriate opto-electronic properties high chemical stability, as well as low cost and low toxicity.
- (d) Produce an inorganic hole transport layer.
- (e) Realise the NW-based 3D-device architecture as suggested by the materials characterization, experimental measurements and simulations.
- (f) Characterise and extract critical parameters of the all-inorganic solar cell to support further materials and process optimization.
- (g) Improve the state-of-the-art efficiencies of similar solar cell types.

The project duration was 31 months and was organized in 6 workpackages (WPs) (apart from project management). Except from WP1 which concerned simulations and solar cell design, each workpackage from WP2-WP5 concerned a different material component. Every single component is crucial for the functionality of the cell as a whole. At the same time, the know-how related to each component can be applied to other application fields within the spectrum of activities of the project partners. This means that even incremental advances in specific WPs represent scientific added value for the project partners. WP6 concerned characterization of the complete cell and as such it played a key role where the synergy of the different material components was put under test and further steps for the cell improvement were decided.

In the following section we describe the technical progress achieved in each project workpackage.

Technical progress description

Transparent electrodes

One of the main tasks in AIT was to develop transparent electrodes on glass that combine high optical transparency and low resistivity, as well as appropriate texture and surface grain morphology to allow the growth of high quality ZnO nanowires atop. Their thermal stability is also relevant, since a significant thermal budget is often required at different stages of the solar cell's fabrication. All investigated transparent electrodes were deposited by DC magnetron sputtering, without substrate heating and at various power densities and Ar pressures. Table 1 summarizes deposition parameters and electrode properties in terms of resistivity and transparency. In the following, ITO stands for In_2O_3 doped with 10 wt.% SnO_2 , whereas AZO for ZnO doped with 2 wt.% Al_2O_3 . The layer thickness in nm is denoted as subscript after the layer.

Transparent electrode	Sputter Power density (W/cm^2)	Sputter Ar pressure (μbar)	Resistivity (ρ) ($\Omega \times \text{cm}$)	Average transmission (T_{av}) 380-750 nm	Haacke quality factor* T_{av}^{10}/R_s (Ω^{-1})
ITO ₂₀₀	1.48	1	2×10^{-4}	84.0%	0.017
AZO ₅₀₀	1.97	1	1.5×10^{-3}	85.2%	0.0073
AZO ₅₀ /Au _x /AZO ₅₀ x=5,7,9	AZO: 1.97	AZO : 1	x=5: 3.2×10^{-4}	x=5: 85.6%	x=5: 0.0075
	Au: 0.44	Au : 2	x=7: 1.9×10^{-4} x=9: 1.3×10^{-4}	x=7: 84.2% x=9: 82.7%	x=7: 0.0100 x=9: 0.0127
AZO ₅₀ /Cu ₅ /AZO ₅₀	AZO: 1.97	AZO : 1	3.2×10^{-4}	82.3%	0.0045
	Cu: 0.44	Cu : 2			

*: The Haacke factor is a figure of merit for transparent electrodes (the higher the value, the higher is the performance)

Table 1: Sputter parameters and properties of the main investigated transparent electrodes.

Fig. 1 presents cross section scanning electron microscopy images from the different electrodes. From all transparent conducting oxides (TCOs) ITO offers unbeatable low resistivity, but indium is relatively scarce (thus expensive) material - therefore, the need to be replaced. Our optimized AZO films have 7-8 times larger resistivity than ITO, but AZO has the advantage of (i) being composed of abundant materials, (ii) having optimal interface quality with ZnO due to the minimal lattice mismatch and perfect energy band alignment, as well as (iii) having a columnar growth mode, which promotes directional growth of ZnO nanowires. XRD investigations showed that, while ITO grows along the cubic bixbyite [111] direction, AZO growth follows the hexagonal [001] with minimal lattice mismatch to intrinsic ZnO.

The use of ultra-thin metals (Au, Cu), in combination with AZO in symmetric sandwich structures (see Table 1) was motivated by the need to decrease the resistivity of AZO single layers without compromising transparency, while maintaining the advantages of the AZO interface to the ZnO NWs grown atop. Indeed, the employment of these metals led to a reduction of the resistivity to levels even below the one of ITO, without loss in transparency^{6,7}. Moreover, the thermal stability of AZO/(Au, Cu)/AZO upon heating in air up to 300°C, is far superior to the one of AZO⁷. This is because the resistivity of the sandwich electrode is mostly determined by the ultra thin metal, which is relative insensitive to temperature.

Atomic force microscopy (AFM) investigation, revealed large differences between the grain structures of the electrodes. The ITO grain morphology distinguishes itself by cauliflower-like, grain-

subgrain structures, whereas AZO-based electrodes have “rounded” grains with grain size which increases with the film thickness. As a result AZO/(Au, Cu)/AZO electrodes have significantly smaller grain size and roughness than single AZO layers of comparable resistivity. In WP3 we will see that grain size largely determines the ZnO NW morphology.

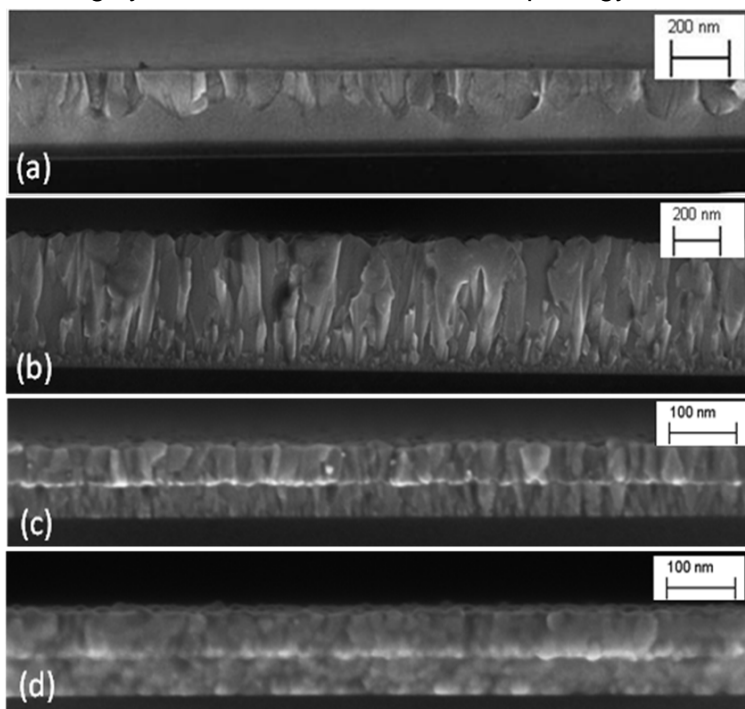


Fig. 1: Cross section SEM images from: (a) ITO_{200} , (b) AZO_{500} , (c) $AZO_{50}/Au_5/AZO_{50}$ and (d) $AZO_{50}/Cu_5/AZO_{50}$ electrodes.

Another strategy to deal with the shortcoming of indium would be to use a more material-economic way to fabricate patterned ITO electrodes, as it is given by structuring and etching of ITO covered substrates. Such possibilities include deposition from nanoparticle solutions, e. g., by inkjet printing.⁸⁻¹¹ Since electrodes from ITO nanoparticle inks usually suffer from low conductivity, improvements are required, which have been suggested to be obtainable by optimizing particle size distributions and composition homogeneities.¹¹ While such efforts are given in literature for ITO nanoparticle inks,⁸⁻¹¹ within this project the JKU has developed another procedure towards a material effective fabrication of nano-patterned ITO electrodes, based on: (i) the synthesis of monodisperse indium and indium tin ($In_{1-x}Sn_x$) colloidal nanocrystals (NCs) with desired size and composition, (ii) the preparation of nanosized patterns from $In_{1-x}Sn_x$ NCs on structured substrates, and (iii), oxidation of the NC patterns to convert the $In_{1-x}Sn_x$ NCs to compact, conductive, and transparent ITO electrodes.

Due to the lack of appropriate synthesis recipes for colloidal $In_{1-x}Sn_x$ NCs in the literature, we introduce a novel synthetic method. It is based on the hot-injection of mixtures of indium and tin silylamide salts into a coordinating solvent. The nucleation rate and thus the final size of the NCs are controlled by a second injection, containing small amounts of strongly reducing super-hydride. Adding lithium-silylamide results in extremely monodisperse NC batches, exhibiting a strong tendency to form ordered superstructures upon slow destabilization or solvent evaporation (Fig. 2 left). These pronounced self-assembly properties of indium and $In_{1-x}Sn_x$ NCs makes the 3-step approach towards ITO electrodes advantageous in respect to the preparation of electrodes directly from ITO-nanoparticle solutions or inks, which suffer usually from size, shape, and composition inhomogeneity.⁸⁻¹¹ On one hand, ordering leads to a minimum of voids between the NCs, and high space filling factors can be obtained in simple drop casted films, which should finally improve the film conductivity. On the other hand, the narrow size

dispersion allows also the fabrication of nanosized electrodes with dimensions down to the size of a single NC, as is demonstrated to be feasible by making use of the “damascene” process.¹²

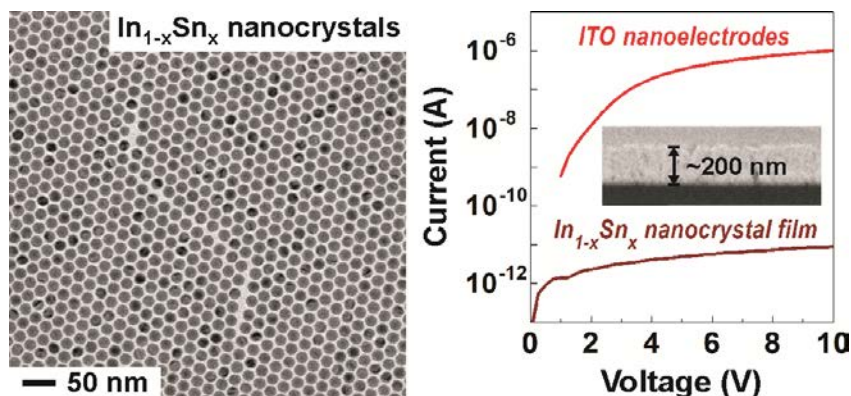


Fig. 2: (Left) Monolayer of monodisperse $In_{1-x}Sn_x$ nanocrystals. (Right) Oxidizing the nanocrystal layer increase and thus converting the $In_{1-x}Sn_x$ to ITO increases the conductivity by 6 orders of magnitude. The inset shows a cross section of the ITO nanocrystal layer.

The oxidation of the NCs is performed by an oxygen plasma, which does not only convert the $In_{1-x}Sn_x$ NC films into ITO electrodes, but also allows interesting insights into the oxidation process itself. The oxidation results in an increase of NC diameter, partly due to an increase of the lattice parameter, but mostly due to the formation of hollow cavities in the NCs centers, caused by the nanoscale Kirkendall effect.¹³ While the plasma treatment also causes the NC assemblies to become transparent over the whole spectral region, the conductivity is optimized by a further moderate heat treatment performed in air, as is also a standard for electrodes prepared from ITO nanoparticles.^{10,12,13} The conductivity, measured in homogeneous thin films obtained by our method, is at least equal to the best values reported so far for electrodes prepared from ITO nanoparticle inks.⁸⁻¹¹ These properties make our ITO electrodes promising for future application and especially it enables, e.g., the development of all-nanoparticle solution-processed optoelectronic devices.

Electrochemical ZnO NW deposition

The electro-chemical deposition (ECD) of nanowire-type structures, without the use of hard templates, requires precise control of the nucleation and growth processes. On one hand it is crucial to avoid homogeneous precipitation within the bulk solution; on the other hand the deposition on the substrate only occurs in a limited range of experimental conditions, close to the precipitation line. In ECD of ZnO NWs, precipitation of ZnO only occurs in close proximity to the electrode/solution interface. The ZnO structure naturally grows only from the conducting electrode surface and thus with inherent electric continuity. The following chemical reactions take place in the aqueous zinc nitrate solution:



ECD allows manipulation of many process parameters (precursor concentration, pH, temperature, deposition potential, additives, solvents) that affect the shape and rate of inorganic growth. In particular, in one of the employed recipes, the supplementation with hexamethylenetetramine (HMTA) increased the quality of the NW array significantly. HMTA serves as additional slow-releasing oxygen precursor. As a consequence of thorough optimization, a deposition parameter regime was defined in AIT for every type of substrate (ITO, AZO, AZO/Au/AZO) that resulted in high-quality ZnO NWs. On ITO substrates, due to the crystal mismatch, ZnO NWs grow non-aligned¹⁴, which leads to pronounced light

loss due to scattering. Below we present the most promising results from ZnO NW growth on AZO and AZO/Au/AZO substrates.

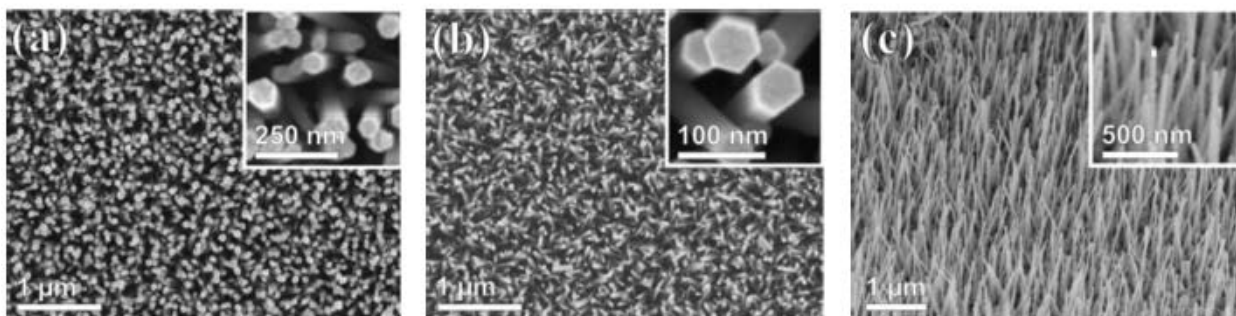


Fig. 3: ZnO NWs on AZO layers with varied thickness: (a) AZO₅₀₀ ($d=65$ nm, $l=1.1$ μm , $AR=17$); (b) AZO₂₅₀ ($d=51$ nm, $l=1.3$ μm , $AR=25$), (c) AZO₁₀₀ ($d=36$ nm, $l=1.8$ μm , $AR=50$).

For the case of AZO substrates, the deposition parameters were adjusted as follows: **electrolyte solution:** aqueous $\text{Zn}(\text{NO}_3)_2$ with HMTA additive; **concentration:** $<1 \cdot 10^{-3}$ mol L^{-1} ; **temperature:** 60 to 80°C ; **potential:** -0.7 to -1 V (relative to Ag/AgCl reference electrode).

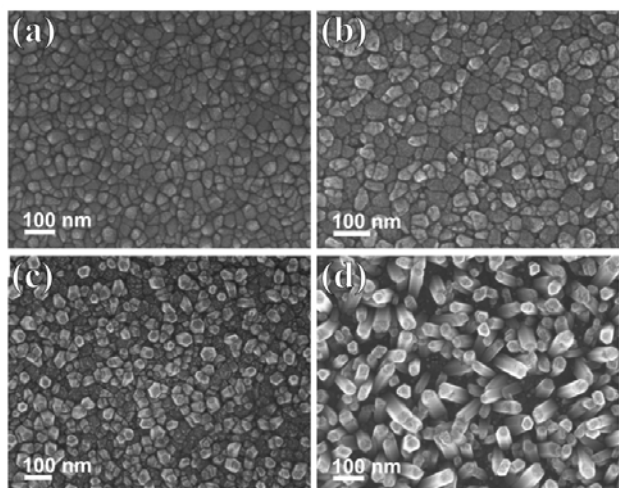


Fig. 4: SEM images during initial ZnO nanowires growth on AZO₂₅₀ at early stages of ECD. (a) 1 min, (b) 5 min, (c) 30 min, and (d) 60 min. ($T = 75^\circ\text{C}$, $E = -1.0$ V).

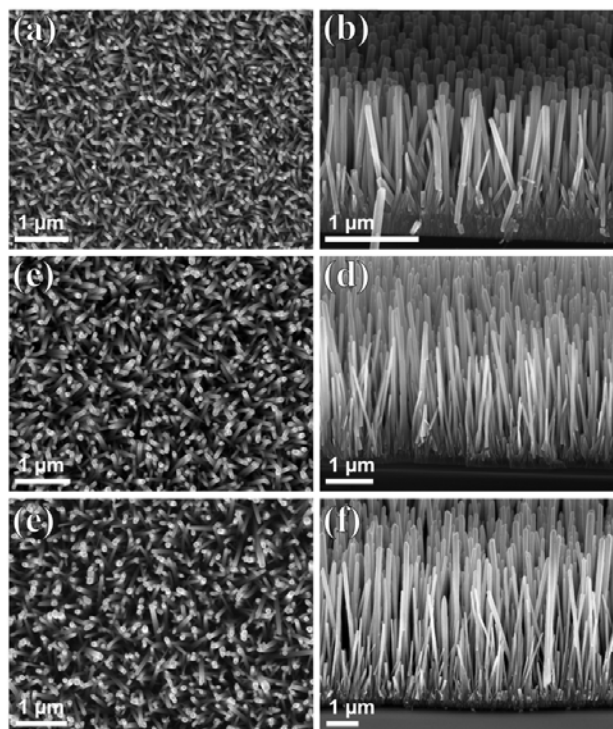


Fig. 5: With the above listed parameters ZnO NWs were deposited successively in three 4h-steps, resulting in structural dimensions correlating with deposition times. The SEM images show top view and cross section of the *i*-ZnO nanowires growth progression after 4h(a,b), 8h (c,d), 12h (e,f).

The deposition of NWs on AZO films of varied thickness (from 50 to 500 nm) showed that the AZO grain size determines the nucleation density, lateral size d , length l , and aspect ratio AR , of the NWs, as shown in Fig. 3 for typical cases. Taking into account the thickness-dependent sheet resistance of the AZO films, an almost linearly increasing correlation between the AZO sheet resistance

and the average length of the deposited NWs was obtained. We also showed the rapid decrease of absolute surface area coverage with NWs from 45% and 37% for the AZO₅₀₀ and AZO₂₅₀, to only 6% and 2% for the AZO₁₀₀ and AZO₅₀, according to the increased sheet resistance of the respective layers. Electrochemically induced nucleation of ZnO growth species therefore appears to be enhanced on thicker AZO films, thus producing denser NW arrays, compared to ZnO NW arrays grown on thinner AZO films with higher sheet resistance.¹⁵

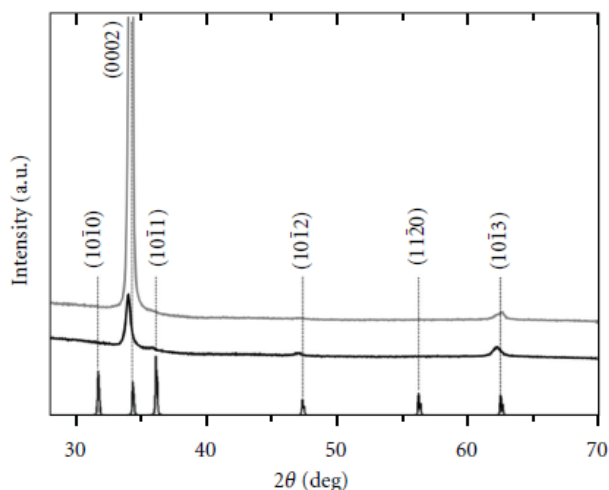


Fig. 6: XRD measurements of AZO₂₅₀ (black line) and AZO₂₅₀/ZnO NW (grey line) samples.

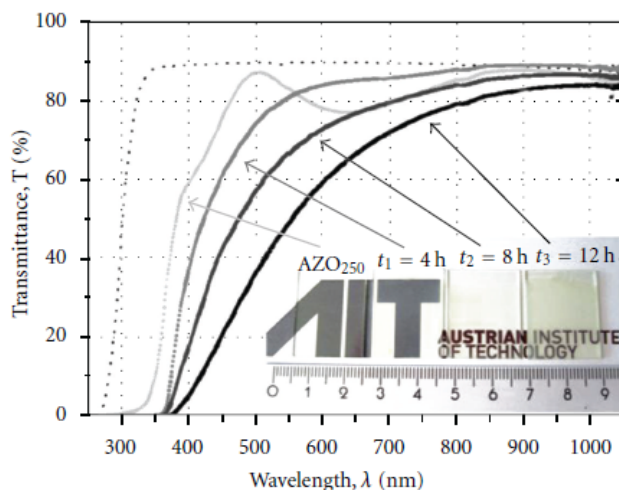


Fig. 7: UV-Vis spectra of plain glass, glass/AZO₂₅₀ and glass/AZO/ZnO NWs after 4h, 8h and 12h deposition.

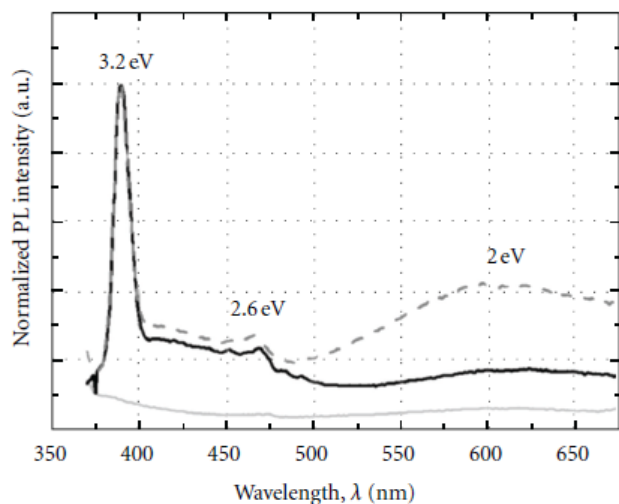


Fig. 8: PL spectra of ZnO NWs grown at 70°C (broken line) and 75°C (black solid line) after a growth time of 4 h. For comparison we include the soda-lime glass/AZO₂₅₀ reference (grey solid line).

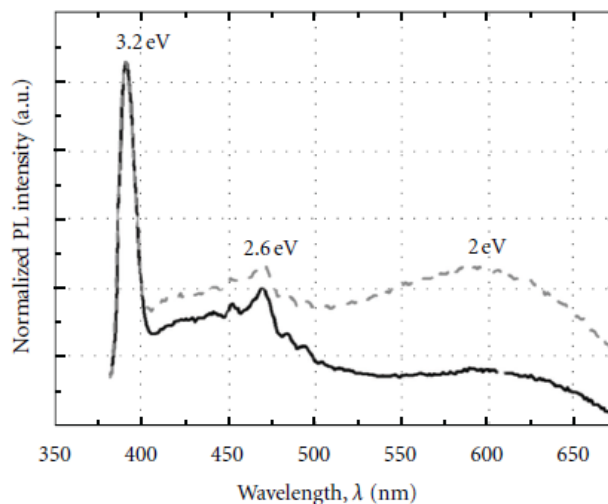


Fig. 9: PL spectra of as grown ZnO NWs (broken grey line) and after annealing at 250°C for 2.5 h (solid black line).

In the SEM images of Fig. 4(a) and 4(b) we see the AZO₂₅₀ surface after 1 min and 5 min of ZnO ECD, respectively. The brighter spots on the surface denote the nucleation sites of the wires, which are indeed defined by the grain boundaries of the AZO film. The NWs continue to grow vertically (Fig. 4(c) and 4(d) for 15 and 60 min ECD respectively), enlarging their aspect ratio with time. Fig. 5 shows the influence of the deposition time on the NW growth. While the NW orientation on ITO is random, on AZO the NWs continue the columnar growth of the TCO film, resulting in hexagonal, highly crystalline structures, elongated along their [001] axis, as shown in XRD measurements (Fig. 6). The pronounced

NW alignment leads to high optical transmission, which decreases, as expected, with increasing NW length, due to enhanced absorption. This is demonstrated in the UV-Vis spectra of Fig. 7, along with photographs of the glass/AZO/ZnO NW samples. The high transparency of the ZnO NW array on AZO is a clear advantage for their solar cell implementation.¹⁵

We also investigated the effect of deposition temperature and post-deposition annealing treatment on the defect density of ZnO NWs. To this end, apart from the structural investigations we performed photoluminescence (PL) measurements, such as the ones shown in Fig. 8 for NWs grown at different solution temperatures. The PL peak at 3.2 eV corresponds to the intrinsic material absorption (corresponding to the bandgap value) and is associated with the good crystallinity and chemical purity of the ZnO NWs. The other peaks are defect-related. The most prominent from them at 2 eV is related to recombination caused by oxygen vacancies in ZnO. The intensity of the defect-induced peaks decreases with increasing deposition temperature. Another means of reducing defects in the NWs is by post-deposition annealing in air, as shown from the PL spectra of Fig. 9.¹⁵

Our investigations of NW growth on AZO showed that the nucleation process does not only depend on the grain size of the layer but also on its sheet resistance. The sandwich electrode provides the same grain size as an AZO₁₀₀ layer, but a sheet resistance which is much lower. As a consequence, the nucleation density on these substrates is approximating full coverage with NWs during the first hour of ECD. Due to competitive growth, the NW density is gradually decreased with deposition time to approx. 60% surface area coverage after 4 h of ECD. The NWs reach an average length of 1.5 μm within this period of time. In Fig. 3.11 we demonstrate a cross section and top view of a NW array on AZO/Au/AZO electrode after 12 h of ECD (renewal of solution every 4 h).

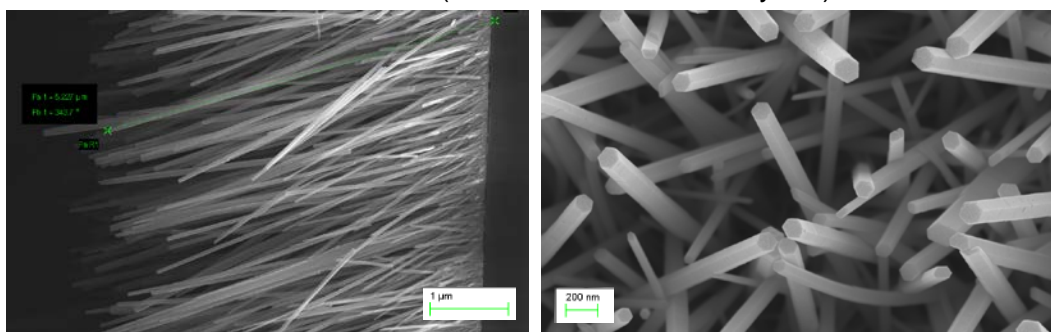


Fig. 8: ZnO NWs electrochemically deposited on AZO/Au/AZO transparent electrode, after 12 h deposition time.

The high crystallinity and the low defect density of these NWs were also certified by XRD and PL measurements. Their morphology and state-of-the-art properties make these wires very promising for implementation in nanostructured solar cells.

Nanocrystals and thin film absorbers

The group at the JKU has developed novel synthesis routes for colloidal nanocrystals, which are potential candidates to be used as solution processable photosensitive materials in solar cells. The materials include Bi_2S_3 and CuInSe (CISE). For the synthesis of Bi_2S_3 nanocrystals we have chosen bismuth(III) tris[bis(trimethylsilyl)amide], $\text{Bi}[\text{N}(\text{SiMe}_3)_2]_3$, as the precursor to deliver Bi. It is injected into an oleylamine solution of elemental S, kept at a temperature of 60°C in inert Argon atmosphere. Here the oleylamine acts also as a ligand and stabilizer, which is attached to the nanocrystal surface. The oleylamine ligands are partly exchanged to oleic acid during the washing procedure. By this synthesis,

typically nanocrystal mean sizes of about 3-4 nm, as is determined by transmission electron microscopy, are obtained (Fig. 9). Tuning the nanocrystal sizes allows the tuning of the nanocrystals energy band gap between 1.25 and 1.6 eV. From the shape of the absorption spectra, close to the band gap, an indirect nature of the band gap can be inferred. Nevertheless, we can obtain photoluminescence from these nanocrystals. For a nanocrystal size of 3.7 nm the PL peak is found at 1.2 eV. This is the first time, that luminescence of Bi_2S_3 nanocrystals is reported.

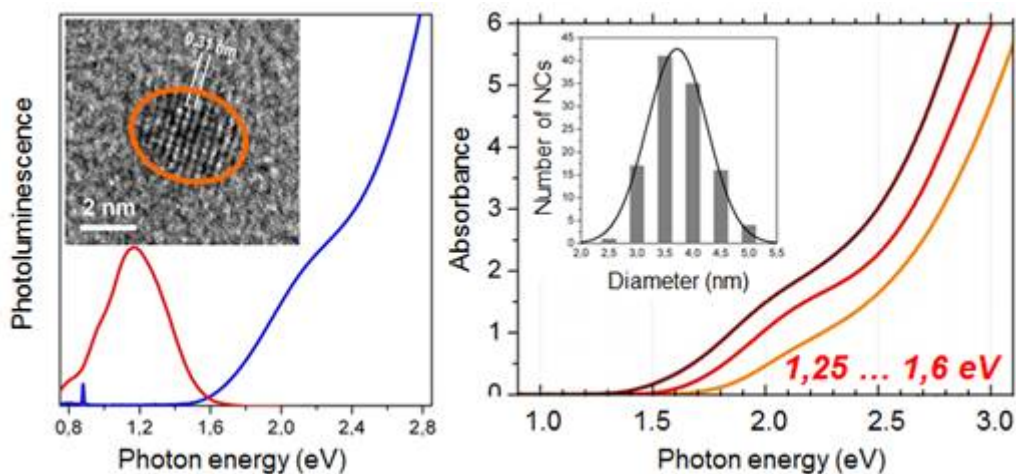


Fig. 9: (Left) Absorbance and photoluminescence spectrum of Bi_2S_3 nanocrystals with a size of 3.7 nm. The inset shows a high resolution TEM image evidencing the mono-crystal nature with a lattice spacing corresponding to that of bulk Bi_2S_3 . By size control the absorption onset is tuned between 1.25 and 1.6 eV. The inset shows a size distribution with a standard derivative of 13.9 %.

While achieving infrared luminescence and size control from Bi_2S_3 nanocrystals can be considered as a good result, the drawback of this material which hampers any application of it in devices is its sensitivity to air. The photoluminescence is obtained only for fresh material and it fades away relatively fast. Also the colloidal stability of this material is significantly worse as compared to other colloidal nanocrystals. Thus we attempted to synthesize another material for the same spectral region.

In particular we have chosen Copper Indium Selenide (CISe) by making use of the precursors CuCl and InCl_3 , dissolved in the coordinating solvent trioctylphosphine (TOP). A mixture of lithium silylamide in TOP and TOPSe, the precursor delivering the Se, is injected in this synthesis. Interestingly the size of the nanocrystals is regulated by the amount of silylamide, as well as by the growth temperature. For the smallest nanocrystals rather irregular shapes are observed and high resolution images reveal also the presence of defects in the nanocrystals (Fig. 10). By increasing the size, a shape change is observed towards rather pyramidal species. The composition of the nanocrystals, determined by energy dispersive X-ray spectroscopy, suggests them to be $\text{Cu}_2\text{In}_4\text{Se}_7$ with a chalcopyrite crystal structure. These nanocrystals are luminescent

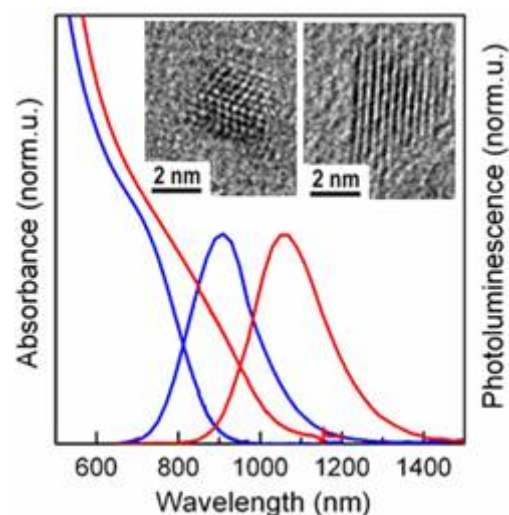


Fig. 10: Absorbance and photoluminescence spectra of $\text{Cu}_2\text{In}_4\text{Se}_7$ nanocrystals with two different sizes. The inset shows high resolution TEM images of the smaller and larger CISe nanocrystals.

and their emission can be tuned by their size to show peak intensities between 900 nm and 1100 nm. The photoluminescence decay time is found to be on the order of 150 ns. The quantum yield is about 6%, which is considerably better than the Bi_2S_3 , but it is still only 1/3 as compared to the highest values we measure for PbS nanocrystals in the same spectral region. Applying a ZnSe shell could further improve this value, however, for applications in solar cells such shells would be counterproductive.

JKU also tested the performance of colloidal nanocrystals as active materials in solar cells. For that purpose PbS nanocrystals were used due to their high photoluminescence yield and good stability in air. To obtain high photocurrents it is crucial to replace the insulating oleic acid ligands on the nanocrystal surfaces by shorter species. This is performed in a layer-by-layer manner by depositing PbS nanocrystals from solution by spin casting, and subsequently rinsing the sample in benzene-dithiol acting as cross linker between the nanocrystals. By depositing in this way a PbS film on an ITO electrode and covering the structure with an metallic top electrode, a solar cell was demonstrated with a high power conversion efficiency close to 4%¹⁶. Reproducing this technology by making use of the ZnO wires as bottom electrode, however, resulted in no measurable photocurrents. This absence of photocurrent could be caused on one hand by a technological problem, like inhomogeneous deposition of the nanocrystals on the wires, or shorts between bottom and top contacts, which we could not rule out by 100%. On the other hand, also there might be also physical reasons which could hamper the operation of a solar cell, like an unfavourable band alignment between the conduction bands of the used active material and that of the electrodes. To prove if the second is the case, transient absorption measurements have been performed, as a measure for the charge transfer between PbS nanocrystals as photosensitizer and the electrode material. In a system where charge transfer between PbS nanocrystals and an electron acceptor (PCBM) takes place, the decay time measured by transient absorption is drastically decreased (Fig. 11 (left)). For the combination PbS nanocrystals on ZnO wires, however, exactly the same transient absorption spectra are measured as for PbS nanocrystals just deposited on glass (Fig. 11 (right)). This observation gives strong evidence that there is no charge transfer between PbS and ZnO wires, which explains the absence of any photocurrents in a diode structure.

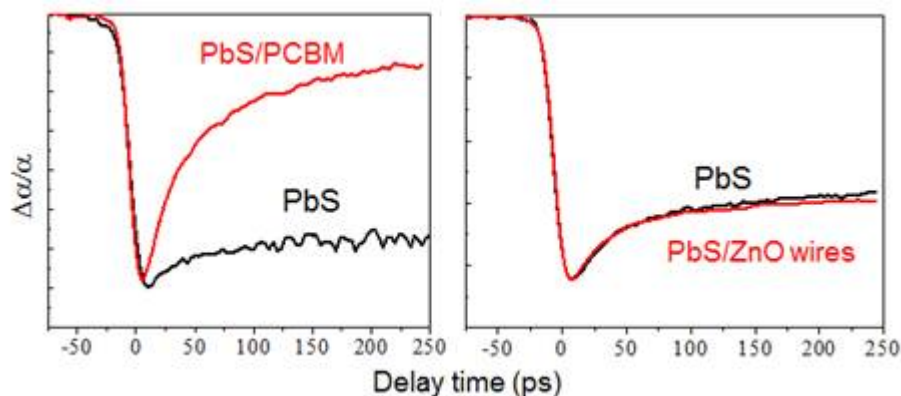


Fig. 11: Transient absorption measured on PbS nanocrystals, on nanocrystals combined with an electron acceptor (PCBM- left) and on a nanocrystal film deposited on ZnO wires (right).

Concerning thin film absorbers, cupric oxide (CuO) was sputter-deposited at 1.75 W/cm² sputter power density, 80/20 Ar/O₂ mixture and sputter pressures between 1 and 50 μbar. The films were highly columnar, with resistivity ranging from approx. 20 Ωcm to 10⁴ Ωcm (measured in freshly deposited films). From UV-Vis measurements of the optical transmission versus wavelength, an indirect bandgap of 1.2 eV was extracted for CuO, which is in agreement with literature values¹⁷ and originates from Cu-3d orbitals forming the two bottom conduction bands and the top valence band. Depending on the sputter pressure, bandgap values ranged from 1.1 to 1.3 eV. A linear fit could be also produced with $n=2$ (Fig. 12), from which we yielded a direct optical transition at 3 eV, arising from the low-lying oxygen-2p band to the conduction band.¹⁷

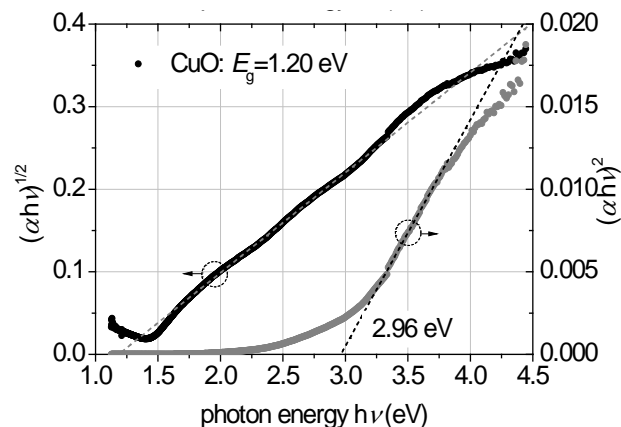


Fig. 12: Extraction of the CuO indirect bandgap (full black dots) and of the direct optical transition gap (full grey dots).

Extensive XRD investigation was conducted to verify the crystal phase of the absorber (tenorite). This was done by means of specular XRD and by highly sensitive techniques such as grazing incidence X-Ray diffraction (GIXD), for single CuO layers on glass or for heterojunctions, like the measurements in Fig. 13. Our investigations showed that for most cases the layer is dominantly composed of cupric oxide phase, with traces of cuprous oxide slightly above the detection limit (2-3 at. %).

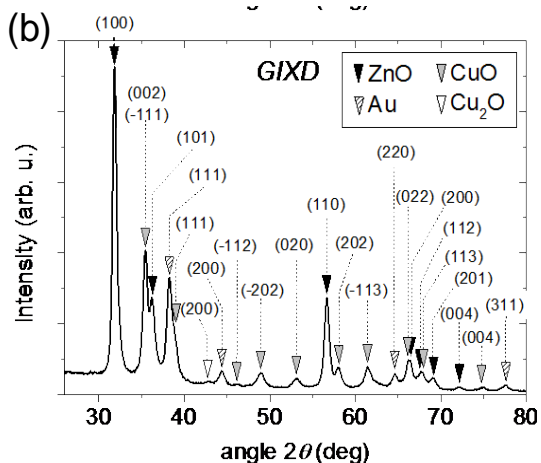


Fig. 13: Grazing incidence surface diffraction from the sample: glass/ AZO₂₁₀/ ZnO₁₀₀/ CuO₂₀₀/ NiO₂₀/ Au₅₀.

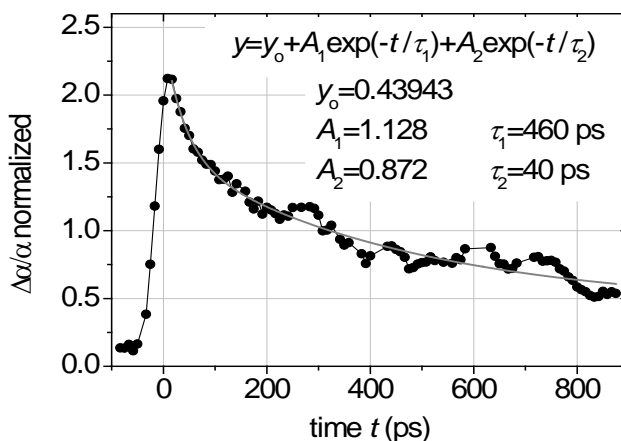


Fig. 14: Transient absorption measurement with the fitting for the extraction of the carrier lifetime in a CuO layer on glass.

For a layer with a resistivity of 24 Ωcm, Hall measurements yielded p-type conductivity with carrier density of $N=7.5 \times 10^{16} \text{ cm}^{-3}$ and mobility of $\mu=3.45 \text{ cm}^2/\text{Vs}$. Moreover, we have, for the first time in the literature, determined the carrier lifetime for the CuO film from pump-probe transient absorption experiments¹⁸. A 532 nm laser pumped electron-hole pairs into the film following absorption. A probe pulse from a 1064 nm laser arrived at the sample at a variable time following the pump and the differential absorption of the sample, related to the carrier population, was monitored as a function of the delay time. The measurement is shown in Fig. 14, where $\Delta\alpha/\alpha$ is the normalized absorption differential. The data were fitted with a bi-exponential curve, yielding two characteristic decay time constants for the

carrier population in the CuO film: $\tau_1=40$ ps and $\tau_2=460$ ps. Combining τ_2 with the mobility value we have extracted earlier, we yield a carrier diffusion length ($L=(\tau\mu kT)^{1/2}$) of approximately 100 nm.

The reactive sputtering of the Cu target with lower oxygen content in Ar (10%), led to the formation of cuprous oxide, as verified from XRD measurements, similar to the ones presented above for CuO. Sputtered Cu₂O films are microcrystalline, as shown from SEM images in contrast to the CuO films which have a pronounced columnar growth. From absorption measurements, the bandgap of sputtered Cu₂O was found to be 2.0 eV (direct).

In another approach, highly crystalline Cu₂O thin-films were grown at 40-60°C by ECD. The source materials were copper sulfate hydrate (CuSO₄) and lactic acid (C₃H₆O₃) to which sodium hydroxide (NaOH) was added to adjust the pH. After the mixture was stirred for several hours, Cu₂O was deposited galvanostatically at current densities ranging from -0.1 mA cm⁻² to -1.2 mA cm⁻² for varying deposition times. Potential-time curves were monitored during the deposition process for growth control. For all current densities and substrates the resulting film was cuprous oxide without traces of cupric oxide or metallic copper. In Fig. 15 we present XRD characterization from samples with Cu₂O absorber deposited on glass/AZO₂₅₀/ZnO NW substrates.

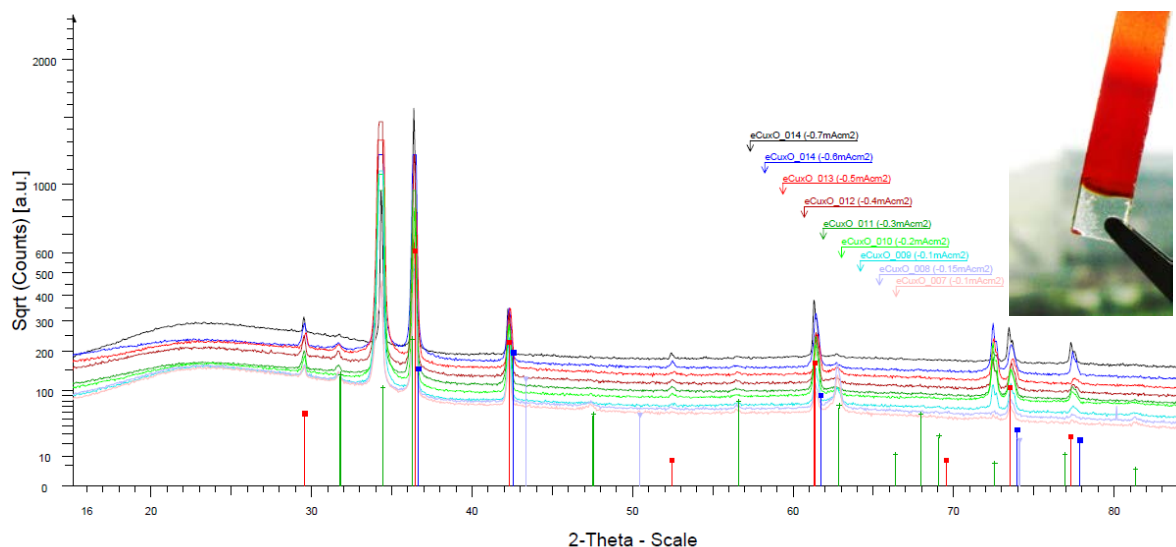


Fig. 15: XRD characterization of ECD grown Cu₂O on glass/AZO/ZnO NWs at different current densities. Peak positions are marked with (a) red for Cu₂O, (b) green for ZnO, (c) blue for CuO, (d) violet for metallic Cu. The inset shows a photo of an ECD Cu₂O layer.

Hole transport layer

During the project we have concentrated on the development of NiO, a large bandgap, *p*-type semiconductor. The layers were deposited from a ceramic NiO target by RF sputtering in reactive Ar/O₂ gas. Optimum and reproducible layer properties were obtained for the highest available O₂ content of 20%. Thicknesses of 10-40 nm were employed, which were shown to improve the photovoltaic properties of the CuO and Cu₂O-based cells. XRD characterization of the NiO layers on plain glass and on the complete cells has shown that the material is amorphous. In Fig. 16 we present the transmittance versus wavelength for a 40 nm film and the extraction of a direct bandgap value of 3.5 eV, in accordance with what expected from the literature. Moreover, a residual optical absorption in the visible and near-IR spectrum, attributed to structural defects in the film, precludes a fully transparent state. The resistivity of NiO was measured at 40 Ωcm.

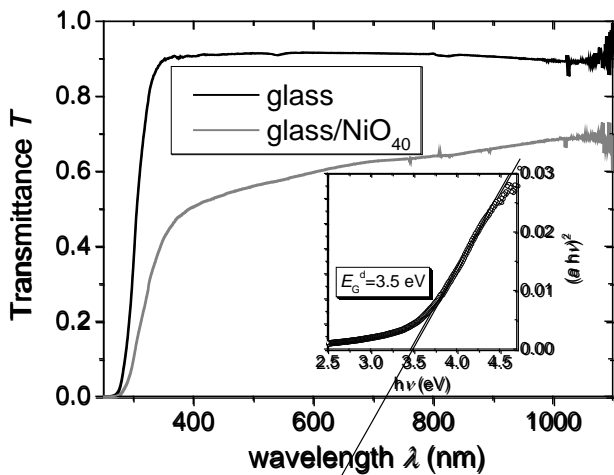


Fig. 16: UV-Vis transmittance vs. wavelength for a 40nm-thick NiO film together with the Tauc plot for the bandgap extraction.

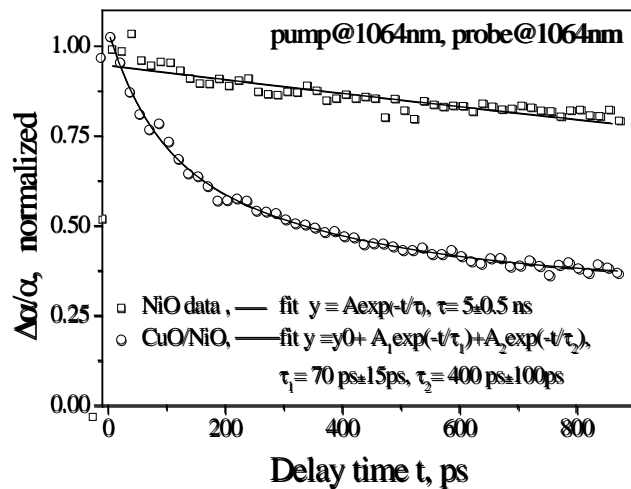


Fig. 17: Transient absorption measurements for the extraction of the photogenerated carrier population decay time in NiO and NiO/CuO.

NiO was further characterized by pump/probe experiments in order to extract the carrier lifetime in the material and monitor charge transfer phenomena between NiO and the CuO absorber. The carrier population upon excitation of a NiO single layer at a wavelength of 1064 nm was found to decay with a characteristic time constant of $\tau=5$ ns (Fig. 17). Interestingly, the carrier decay time for the glass/NiO/CuO sample was significantly reduced. A biexponential fit of the data gives in this case $\tau_1=70$ ps and $\tau_2=400$ ps. This reduction of carrier lifetime suggests charge transfer between NiO and CuO.

The p-type characteristic of the NiO layer was demonstrated by the fabrication of *n*-ZnO/*p*-NiO heterojunctions. More specifically, multilayers of: glass/AZO₂₅₀/ZnO₁₀₀/NiO_{x=20,40}/Au₁₀₀ were electrically characterized by current-voltage measurements. The IV is diode-like with a high rectification.

Solar cell fabrication and characterization

For the evaluation of the proposed materials different architectures of solar cells have been investigated: planar thin film solar cell, as well as 3D type, employing NW arrays. Here we will present a summary of our main results.

A big part of our investigations concentrated on sputter-deposited planar ZnO/CuO heterojunctions, with the purpose to study the properties of this absorber in a simple solar cell architecture, before proceeding into the implementation of a 3D NW electrode. From the simulations we extracted that a CuO thickness of around 1 μm would be sufficient to absorb most of the solar spectrum light, while it was also shown that a reflecting top Au electrode is beneficial in terms of light absorption, especially in the case of thinner absorber films. In one set of experiments we characterized the PV performance of solar cells as a function of the CuO thickness (keeping the other layer thicknesses constant). We chose the following general architecture for the heterojunctions: glass/AZO₂₁₀/ZnO₁₀₀/CuO_x/NiO₂₀/Au₄₀₀, with $x=400, 500, 600, 900$ nm. A cross section SEM image and a photograph of such a sample is shown in Fig. 19. The CuO layer has indeed a pronounced columnar growth and lacks compactness, as voids are observed between the columns. Fig. 18 summarizes the PV properties.

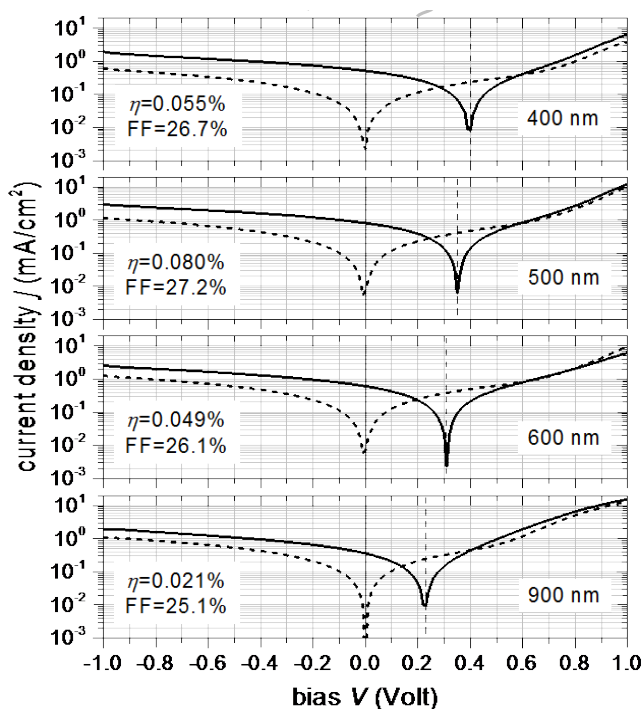


Fig. 18. *j-V characteristics in dark and under illumination for solar cells with different CuO thickness.*

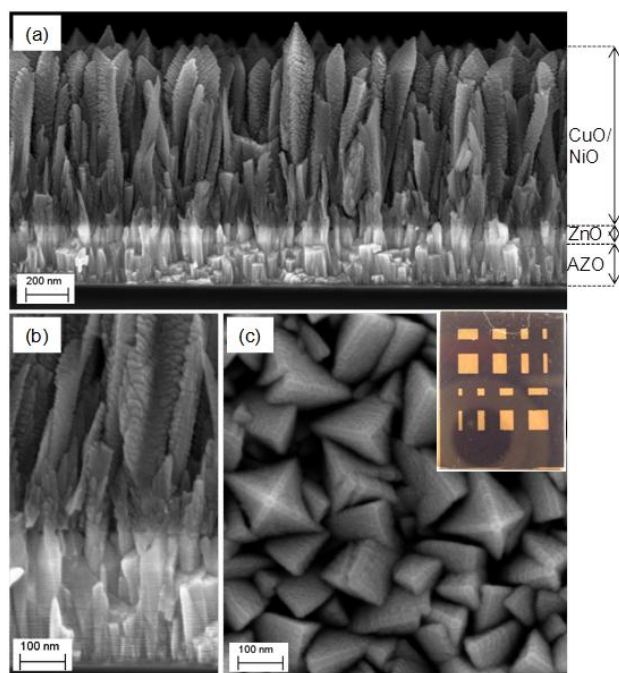


Fig. 19: (a) and (b) Cross section SEM images of the sample: glass/AZO₂₁₀/ ZnO₁₀₀/ CuO₉₀₀/ NiO₂₀. (c) Top surface SEM image from the same sample and a photo of the heterojunction with the Au contacts.

Under illumination, maximum short circuit current density of $j_{sc}=0.85 \text{ mA/cm}^2$ is obtained for $x=500 \text{ nm}$. Thinner or thicker absorber films lead to a decrease of j_{sc} (see Fig. 18). In parallel, the open circuit voltage, V_{oc} , constantly declines from a value of 400 mV for $x=400 \text{ nm}$ to 210 mV for $x=900 \text{ nm}$. The fill factor (FF) also maximizes for $x=500 \text{ nm}$ at 27.2%. Finally, the power conversion efficiency assumes a maximum of $\eta=0.08\%$ for $x=500 \text{ nm}$. This value is on par with the best efficiency reported in the literature for CuO absorber, in a cell composed of CuO nanowires, thermally grown from a Cu sheet and then coated with ZnO¹⁹. We would also like to point out the effect of NiO in the PV characteristics. Its presence as an anode interfacial layer was found to enhance both j_{sc} and V_{oc} . More specifically, for solar cells with $x=500 \text{ nm}$, the employment of 20 nm NiO gave rise to an almost 2-fold increase of j_{sc} and an increase of the V_{oc} by up to 120 mV. From the analysis of the above results it was concluded that the ZnO/CuO heterojunction PV performance is compromised by the poor carrier lifetime in CuO.

The sputter-deposition of CuO on a NW electrode led to poor penetration of the material, as expected from the high directionality of the deposition technique. Nevertheless, the short circuit current density for a nominally 900 nm-thick CuO film was 1.2 mA/cm^2 , the open circuit voltage 200 mV and the fill factor 27%, which yielded a power conversion efficiency of 0.07%, which is larger than the one achieved for the planar solar cells with the same CuO thickness.

In the following, we have focused our efforts in Cu₂O, since better photovoltaic properties were achieved compared to CuO.

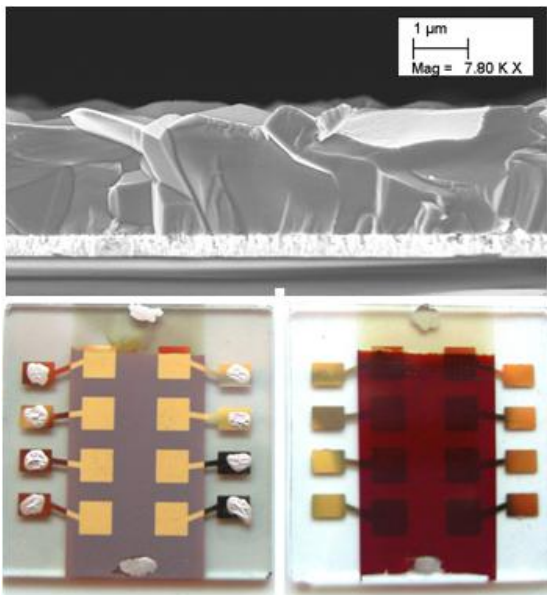


Fig. 20: Cross section SEM image of an ECD- Cu_2O heterojunction solar cell together with photos from the top and bottom glass side of Cu_2O absorber cells (glass substrate of 2.5×2.5 cm).

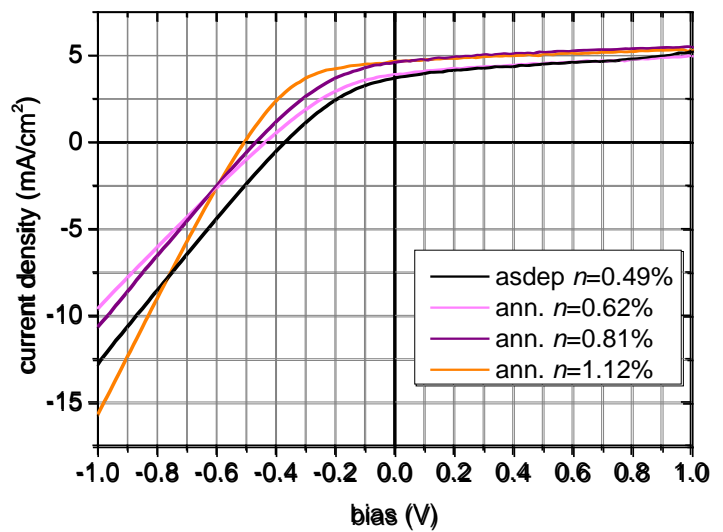


Fig. 21: IV curves under illumination measured for solar cells with ECD Cu_2O after post-deposition treatment at different temperatures.

Planar, thin film solar cells employing electrochemically grown Cu_2O absorber were fabricated and characterized. The most promising heterojunction composition consisted of an AZO-based bottom electrode combined with intrinsic ZnO film. The Cu_2O was deposited atop, followed by the sputtering of top contacts. A cross section SEM image of such a multilayer (without the Au top contact) is shown in Fig. 20, demonstrating the large Cu_2O crystals produced by ECD.

The power conversion efficiency of these cells under AM1.5G illumination is approx. 0.5%, having a short circuit current of 3.71 mA/cm^2 , an open circuit voltage of 370 mV and a fill factor of 36%. Our latest experiments nevertheless showed that the PV performance can be greatly enhanced by post-deposition thermal treatment. The obtained IV curves under illumination are shown in Fig. 21. The performance of the cell reaches 1.12% efficiency with a short circuit current of 4.7 mA/cm^2 , open circuit voltage of 505 mV and fill factor of 47.5%. The improvement of the efficiency is partially due to the reduction of the series resistance and the increase of the solar cell shunt resistance. The achieved efficiency of 1.12% is one of the best values reported in the literature for electrochemically grown Cu_2O absorber. Most interestingly, Cu_2O based cells are extremely robust and do not alter their properties even months after their fabrication without encapsulation.

The electrochemically grown Cu_2O was implemented in a 3D ZnO NW electrode. The absorber material penetrates efficiently inside the voids of the nanostructures, as shown in the SEM images of Fig. 22. The electrical characterization in Fig. 23 shows diode like characteristics with large rectification in dark. For the investigated cells under illumination we obtained an efficiency of 0.32%, with a short circuit current of 5 mA/cm^2 , open circuit voltage of 180 mV and fill factor of 35.4%. Although the short circuit current density is larger than the one of as-deposited planar samples (attributed to the enhance surface of the nanowire electrode), the open circuit voltage is much lower, which is attributed to the enhanced recombination in the ZnO NW / Cu_2O interface and the larger series resistance.

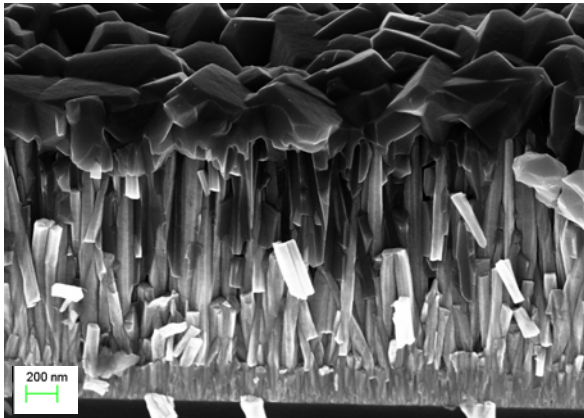


Fig. 22: Solar cell of AZO/ZnO NWs/Cu₂O

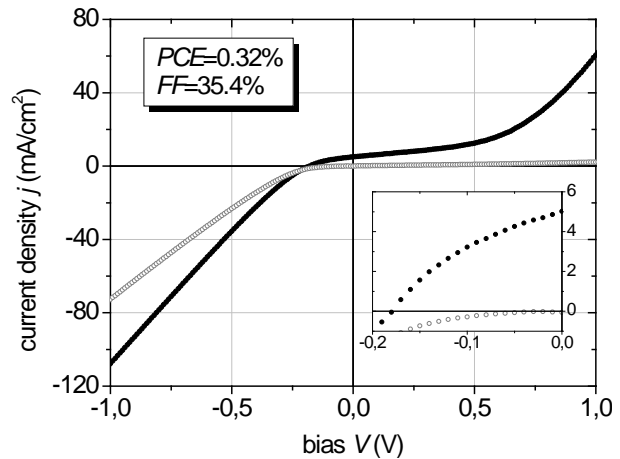


Fig. 23: *j*-V curves of the nanowire solar cell in dark and under AM1.5G illumination.

Our efforts towards a 3D solar cell extended also to other approaches. One of the most promising ones we believe it is the fabrication of ZnO/Cu₂O core/shell structures (Fig. 24), which would be the ultimate choice for an extremely thin absorber type of cell. Such nanostructures were achieved on specific electrodes and ECD parameters, which induced the growth of Cu₂O in a form of shell around the nanowires. Unfortunately, we faced problems when contacting this type of structures with a top electrode, as a direct contact between the ZnO NW tips and the top contact led to shorted cells. Further efforts to contact these cells have been undertaken.

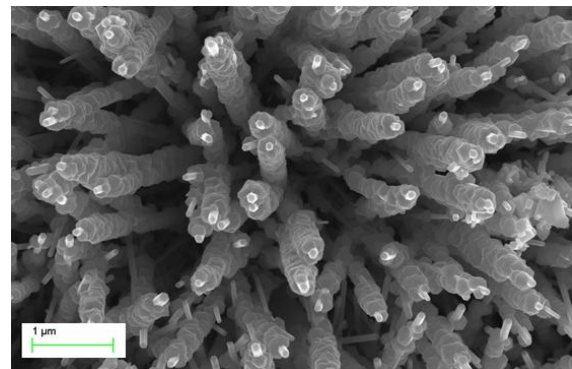


Fig. 24: ZnO NWs enveloped by a shell of electrodeposited Cu₂O.

The sputter-deposition of Cu₂O on the NW electrode led to the formation of club-like structures, with reduced penetration of the material inside the nanostructure voids. Nevertheless, the void filling was a bit better than the CuO case, since cuprous oxide grows microcrystalline (Fig. 25). The power conversion efficiency in this case was 0.18%, with a short circuit current density of 2.5 mA/cm², open circuit voltage of 260 mV and fill factor of 28%.

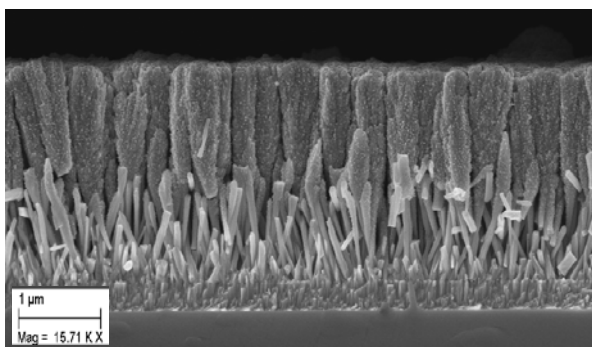


Fig. 25: Sputtered Cu₂O on AZO/ZnO nanowires.

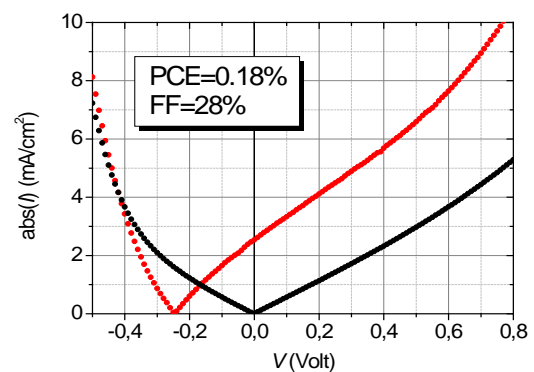


Fig. 26: *j*-V characteristics of sputtered AZO/ZnO NWs/Cu₂O/NiO/Au solar cells in dark and under AM1.5G

illumination.

Much of our effort concentrated on the employment of colloidal nanocrystals on the NW electrode. Our first attempts used PbS NCs, since this material was readily available, with well characterized properties and stability in air. The colloid was brought on the NWs by different techniques, such as spinning, dip coating, injecting. One of the main problems was the hydrophobic NW surface that impeded the penetration of the colloidal solution inside the voids of the nanostructure. Finally we have succeeded in doing so by injecting the colloidal solution in several steps, after processing the NW surface. The linker molecule in this case was oleic acid. After bringing Au contacts by sputtering, we characterized the cell taking IVs in dark and under illumination. Although rectifying IVs were obtained, there was no PV characteristic. Many reasons could cause this. Our investigations arrived to the conclusion that the ZnO/PbS interface impedes charge transfer. On the other hand, the poor stability in air of the Bi₂S₃ NCs and the low quantum yield of ClSe NCs did not allow their implementation in a solar cell of this kind.

- [1] B. O'Regan and M. Grätzel, *Nature* 353 (1991) 737.
- [2] K. Tennakone et al., *J. of Phys. D: Appl. Phys.* 31 (1998) 2326.
- [3] I. Kaiser et al., *Sol. Energy Mater. Sol. Cells* 67 (2001) 89.
- [4] C. Levy-Clement et al. *Adv. Mater.* 17 (2005) 1512.
- [5] K. S. Leschkies et al., *Nano Lett.* 7 (2007) 1793.
- [6] T. Dimopoulos, G.Z. Radnóczy, B. Pécz, H. Brückl, *Thin Solid Films*, 519 (2010) 1470-1474
- [7] T. Dimopoulos, G. Z. Radnóczy, Z. E. Horvath, H. Brückl, *Thin Solid Films* 520 (2012) 5222
- [8] J. Ba, D. F. Rohlffing, A. Feldhoff, T. Brezesinski, I. Djerdj, M. Wark, M. Niederberger, *Chem. Mater.* 18 (2006) 2848.
- [9] G. Bühler, D. Thölmann, C. Feldmann, *Adv. Mater.* 19 (2007) 2224.
- [10] R. A. Gilstrap, C. J. Capozzi, C. G. Carson, R. A. Gerhardt, C. J. Summers, *Adv. Mater.* 20 (2008) 4163.
- [11] T. Sasaki, Y. Endo, M. Nakaya, K. Kanie, A. Nagatomi, K. Tanoue, R. Nakamura, A. Muramatsu, *J. Mater. Chem.* 20 (2010) 8153.
- [12] G. Chen, M. I. Bodnarchuk, M. V. Kovalenko, G. Springholz, W. Heiss, W. Jantsch, E. Platzgummer, H. Loeschner, J. Schotter, *Adv. Mater.* 22 (2010) 1364.
- [13] Y. Yin, R. M. Rioux, C. K. Erdonmez, S. Hughes, G. A. Somorjai, A. P. Alivisatos, *Science* 304 (2004) 711.
- [14] X. Bubnova, Antun Peić, T. Dimopoulos, S. Abermann, M. Rennhofer, J. Akbarzadeh, H. Peterlik, L. Irusta, P. Ertl 26th European Photovoltaic Solar Energy Conference and Exhibition Proceedings 2011.
- [15] A. Peic, T. Dimopoulos, R. Resel, S. Abermann, M. Postl, E. J.W. List, and H. Brückl, *Journal of Nanomaterials* Volume 2012, Article ID 457904, doi:10.1155/2012/457904
- [16] K. Szendrei, W. Gomulya, M. Yarema, W. Heiss, and M. A. Loi, *Appl. Phys. Lett.* 97 (2010) 203501.
- [17] F. P. Koffyberg, F. A. Benko, *J. Appl. Phys.* 53 (1982) 1173.
- [18] T. Dimopoulos, A. Peić, P. Müllner, M. Neuschitzer, R. Resel, S. Abermann, M. Postl, E. J. W. List, S. Yakunin, W. Heiss, and H. Brückl, accepted for publication in *Journal of Renewable and Sustainable Energy*.
- [19] P. Wang, X. Zhao, B. Li, *Optics Express* 19 (2011) 11271.

Main results and conclusions of the project

The main project's results can be summarized as follows:

- 1) We have developed a variety of transparent electrodes on glass with different opto-electric and structural properties: Sn:In₂O₃ (ITO), Al:ZnO (AZO) and AZO/(Au, Cu)/AZO, upon which we have tested the electrochemical growth of ZnO NWs.
- 2) A novel, solution-based, synthetic method was developed for colloidal ITO NCs, providing a low-cost replacement to ITO films.
- 3) We managed to tailor the growth of ZnO NWs (length, width, aspect ratio, packing density) through the choice of the underlying transparent electrode and by varying the electrochemical deposition parameters and solution components. State-of-the-art structural and optical properties of the NWs were obtained.
- 4) Thin film absorber materials of CuO (cupric oxide) and Cu₂O (cuprous oxide) have been developed by two different techniques: sputtering and electrochemical deposition.
- 5) Two synthesis routes for infrared active colloidal nanocrystals of Bi₂S₃ and CuInSe (CISe), which are potential candidates to be used as solution processable photosensitive materials in solar cells, were developed.
- 6) We have identified the shortcomings of the developed inorganic NCs in terms of long term stability and quantum efficiency.
- 7) NiO thin film HTM was fabricated by sputtering and showed to improve the PV properties of the investigated solar cells.
- 8) We have achieved the highest power conversion efficiency reported for CuO thin film solar cells and uncovered the intrinsic limitations of this material.
- 9) We have come on par with the best reported efficiency for electrodeposited Cu₂O solar cells (1.12%) and achieved one of the best results yet on Cu₂O absorber on ZnO NR electrode.

Outlook - Suggestions

Many of the materials and processes investigated during the SANCELL project worth to be further developed for renewable energy applications.

We believe that electrochemical deposition and hot-injection synthesis are processes with high potential and relevance to low-cost, low-tech PV, which is highly demanded from the market. We also propose further work on abundant, non-toxic and easily manufactured (nano)materials, acquired either by substituting scarce elements in existing semiconductor alloys, or developing new semiconductors. Particularly interesting we find the kesterite Cu₂ZnSn(S,Se)₄ absorber which targets to replace In and Ga in the CIGS technology and has shown very promising results in terms of efficiency (>10%). Also promising are simple binary alloys such as Fe₂S and Cu₂O. Thorough experimental and theoretical investigation of their properties has to take place in order to investigate their photovoltaic potential. In the same line, new organic absorber materials with high long-term chemical stability and efficiency should be developed for low-cost PV.

Another area where future research work should concentrate is the development of low-cost, easily up-scalable processes for 3D nanostructures for light management and electric charge transport. This should go hand-in-hand with the development of deposition processes for conformal growth of thin absorber films and functional layers on 3D structures, such as Atomic Layer Deposition (ALD) and electrochemical deposition. New characterization techniques to probe material interface properties are

also highly demanded. The substrate is also a critical factor for future PV. Cheap, flexible organic or metallic foils can be of great interest especially for the building industry and would permit roll-to-roll fabrication of PV, which is highly cost-effective. Therefore we have to promote the adaptation or development of fabrication processes for flexible substrates.